Nanomaterials for Electrocatalytic Water Activation

A Synopsis of the Thesis to be submitted to the Mangalore University
for the award of the degree of Doctor of Philosophy
in Chemistry

Submitted to

Mangalore University

Department of Chemistry
Mangalagangotri-574 199

By

Alex C

Enrolment no: 178105103
Date of Registration: 03-04-2018
Ref: No.MU/EXB/Ph.D./CR.109/Phy./2019-20/E.13

under the supervision of

Dr. Neena Susan John

Centre for Nano and Soft Matter Sciences
Survey No.7,
Shivanapura, Dasanapura Hobli,
Bangalore – 562 162

May 2022

Preface

The tremendous utilisation of fossil fuels has accelerated the search for alternative renewable energy sources such as solar energy, wind energy, hydro energy, tidal energy, geothermal energy, biomass energy, etc. Hydrogen fuel is a zero-emission, energy carrier with high efficiency (60 %) in the fuel cell, around two times higher efficiency than that obtained through power plants (33 %). Currently, ~95 % of hydrogen gas production is from fossil fuels with a small amount through biomass gasification or electrolysis of water. Production of hydrogen from fossil fuel in most cases releases CO/CO_2 gases into the atmosphere and hence, alternative techniques such as the electrolysis of water and urea have a huge commercial significance.

Catalysts are required for water or urea electrolysis to reduce the activation energy of a electrochemical reaction. In recent days, nanomaterial-based electrocatalysts are rigorously researched due to their unique properties, such as (i) high specific surface area, (ii) a large number of electrocatalytic active sites. These specific properties have a fruitful effect on catalytic activity, so tremendous efforts are ongoing on developing nano-sized catalysts for hydrogen production. Even though many elelctrocatalysts are shown with good activity, a proper understanding of these catalysts for hydrogen production is still lacking. In a catalyst, the number of active sites is considered as a real descriptor for its activity, but deviations are seen in many systems. Identifying proper active sites and synthesizing stable catalysts without activity loss under elelctrochemcial conditions are the major challenges in nanomaterial-based electrocatalysts.

The present thesis deals with the improtance of hydrogen energy and requirements of an electrocatalyst. We have shown a chemical route to stabilise an electrocatalyst for prolonged usage at high current density. The improvement of electrocatalyst activity based on tuning it's redox sites have been discussed in cobalt based systems. The advantage of coordinatively unsaturated nickel oxide based compounds for efficient urea electro-oxidation are discussed and studied.

This thesis is organized into seven chapters. The first chapter gives an introduction to electrochemical water splitting with discussion on electrolysis requirements and the need for cheaper and efficient electrocatalysts. Chapter 2 describes various characterization techniques employed and their working principles for material and electrochemical analysis. Chapter 3

discusses Pd based coordination polymer-graphene composites for sustainable electrochemical hydrogen production. We have explored a coordination polymer for stabilizing Pd nanoparticles with size of 2-5 nm, and show that the stability of the catalyst for hydrogen evolution reaction (HER) improved to 70 h at current density of -300 mA/cm^2. Chapter 4 discusses the oxygen evolution reaction (OER) by earth-abundant Co_3O_4 systems and the identification of the critical factor for significant activity. Two different Co_3O_4 systems are synthesized; one with high oxygen deficiency as Co_3O_{4-x} and another with more Co^{3+} reducibility as there are controversial reports on oxygen deficient metal sites as active sites for OER. We have studied the role of the above key factors competing towards OER activity. The role of active metal sites over ligand influence in various bivalent cobalt phosphorous oxygen systems towards OER is discussed in chapter 5. We have synthesised three different cobalt phosphorous oxygen systems such as $NaCoPO_4$, $Co_{11}(HPO_3)_8(OH)_6$, $Co_3(HPO_4)_2(OH)_2$ and the relationship between Co^{3+} reducibility and OER activity was studied. Chapter 6 discusses the importance of urea electrolysis and surface defective NiO as a catalyst for urea electro-oxidation reaction (UOR). The surface defects of NiO was introduced by novel electron bombardment technique. Further the mechanism of urea electro-oxidation is analysed through impedance spectra studies. Chapter 7 discusses the over all conclusions of various catalysts studied. The studied catalyst activity descriptor, stability, active site enhancement factor and ways of tuning the materials for fruitful applications are presented. The future scope of each studied catalyst with some new questions based on our conclusions are discussed.

Chapter 1: Introduction to Electrochemical Water Splitting and Electrocatalysts

Electrochemcial water splitting is an emerging technology to produce hydrogen. In this technique, the analytes/reactants (eg: H_2O) are subjected to an external potential caused by positively and negatively polarised electrodes. The electrochemical water splitting has advantages of being a clean route with the potential of replacing presently used hydrogen production techniques such as methane and fossile fuel pyrolysis [1].The produced hydrogen has significant commercial values in fuel cells, petroleum refining and ammonia production industries. Currently, the heavily used catalyst for electrochemical water splitting are based on precious metals such as Pt, Ir, Ru, etc,. These catalysts are expensive and restrict the wider application of hydrogen fuel and hence, developing an alternative catalyst for these applications are needed [2,3].

Electrolysis:

The electrochemical decomposition of a compound into its smaller molecules/elements by the application of potential between two electrodes (one acts as a cathode and another as an anode) is called electrolysis. The applied voltage is called as decomposition potential. Water and urea electrolysis hold significant potential for hydrogen production [4].

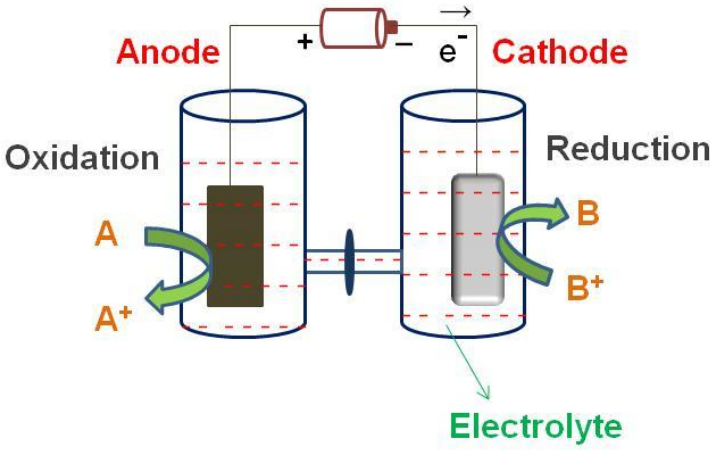

Figure 1: Simple cell set-up for electrolysis.

The simple electrochemical cell set-up has two electrodes with an electrolyte; **Cathode:** The electrode at which the electrochemical reduction reaction happens, **Anode:** The electrode at which the electrochemical oxidation reaction happens and **Electrolyte:** These are mostly

ionic compounds that easily dissociate and participate in an electrochemical reaction (e.g., KOH, H_2SO_4, etc.).

Electrolysis of Water:

Electrolysis of water consists of two half cell reactions, (1) Anodic oxygen evolution reaction (2) Cathodic hydrogen evolution reaction. The standard state water electrolysis needs an overall cell voltage of 1.23 V vs standard hydrogen electrode (SHE) [5].

Anodic oxygen evolution reaction:

In neutral/acidic medium: $2\ H_2O \rightarrow O_{2(g)} + 4\ H^+ + 4e^-$ $E^0 = 1.23$ V

In alkaline medium: $4\ OH^- \rightarrow O_{2(g)} + 2\ H_2O + 4e^-$ $E^0 = 0.401$ V

Cathodic hydrogen evolution reaction:

In acidic medium: $2\ H^+ + 2e^- \rightarrow H_{2(g)}$ $E^0 = 0$ V

In alkaline medium: $2\ H_2O + 2e^- \rightarrow\ 2\ OH^- + H_{2(g)}$ $E^0 = -0.829$ V

Electrolysis of Urea:

The urea electrolysis has two half cell reactions (1) Anodic urea oxidation reaction (2) Cathodic reduction or hydrogen evolution reaction. The standard state urea electrolysis needs an overall cell voltage of 0.37 V vs SHE [4].

Anodic urea oxidation reaction:

It proceeds through two ways (i) Direct urea electro-oxidation, (ii) In-direct urea electro-oxidation.

Direct urea electro-oxidation:

$CO(NH_2)_2 + 8\ OH^- \rightarrow N_{2(g)} + 6\ H_2O + CO_3^{2-}{}_{(ions)} + 6e^-$ $E^0 = -0.746$ V

In-direct urea electro-oxidation:

$CO(NH_2)_2 + 6\ OH^- \rightarrow N_{2(g)} + 5\ H_2O + CO_{2\ (g)} + 6e^-$ $E^0 = -0.46$ V

Cathodic reduction/hydrogen evolution reaction:

$2\ H_2O + 2e^- \rightarrow H_{2(g)} + 2\ OH^-$ $E^0 = -0.829$ V

Fundamental factors which affect the electrolysis:

The main factor which limits the electrolysis of water and urea is over potential. The overpotential is an excess applied potential required to begin the electrochemical reaction practically from its theoretical potential. Among various overpotentials involved, the three important ones are given below [6].

I. Activation overpotential:

It is defined as the potential difference above the equilibrium potential required to overcome the activation energy barrier for an electrochemical reaction.

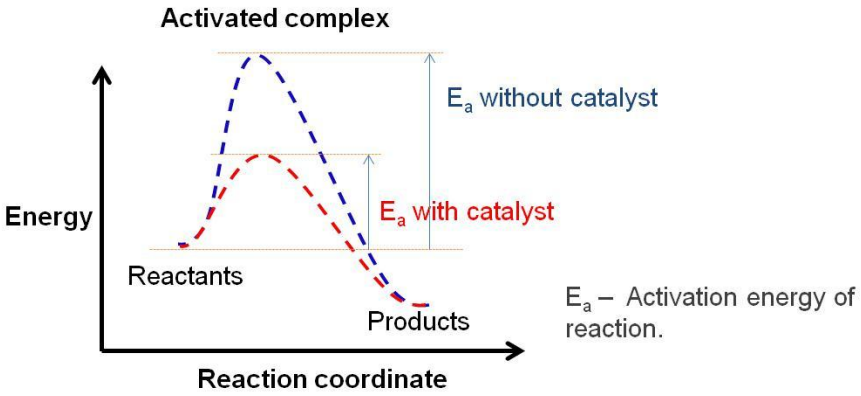

Figure 2: Plot represents activated complex formation and its activation energy (E_a) during electrochemical reaction with and without electrocatalyst.

The above figure represents (Fig. 2) the formation of product from the reactant, through activated complex formation and the energy needed to form activated complex formation is termed activation energy (E_a). The application of potential will supply the energy and it can be reduced using suitable electrocatalysts.

II. Concentration overpotential:

The extra potential needed to bring the charge carrier or reactants towards the electrode for carrying out the electrochemical reaction. During the electrochemical reaction, the amount or concentration of reactants near the electrode gets depleted, and the surface needs more reactants to proceed reaction. In this condition, the rate of reaction depends on the ability of reactants to reach the electrode and can be attained by the application of extra potential, termed as concentration overpotential. The concentration overpotential can be reduced by stirring the electrolyte or using rotator disk electrode for electrochemical reaction.

III. Resistance over potential:

This overpotential is caused by cell design and depends on the distance between cathode and anode. A larger distance between electrodes leads to high solution resistance, which can be resolved by minimising the distance between cathode and anode.

Nanomaterials and catalytic activity:

Materials with one of its dimensions less than 1-100 nm are called nanomaterials. All materials can be synthesised in nanosize, but our interest in nanomaterials is to boost electrochemical hydrogen production. The nanomaterials have the main advantage of high specific surface area, which allows for many exposed catalytic active sites. The active site improvement directly impacts the effectiveness and efficiency of a catalyst electrochemical reaction [7].

The usage of electrocatalysts helps to reduce activation overpotential. This is manifested via altered free energy of key intermediates close to zero ($\Delta G_{ads} \sim 0$) on the catalyst surface. In the case of HER, the intermediate considered is adsorbed hydrogen while during oxygen evolution reaction the O-O bond forming intermediates adsorption energies are considered. In UOR the CO_2 adsoprtion energy is considered for activity improvement.

Chapter 2: Experimental Techniques

X-ray Diffractometer (XRD):

The crystal structures of synthesised electrocatalysts are studied using an X-ray diffractometer (XRD). The measurement is based on Bragg's law (1),

$$n\lambda = 2d \sin\theta \qquad (1)$$

where n = diffraction order (n = 1, 2, 3, etc.,), d = distance between successive layers of atoms which makes diffraction, θ = glancing angle of incident and λ = wavelength of X-ray.

The XRD of all samples were acquired using Rigaku Smart Lab X-ray diffractometer having Cu Kα as X-ray source (λ = 1.5406 Å). Measurements for films were carried out at grazing-incidence diffraction mode [8]. Powder X-ray diffraction was collected in Bragg-Brentano focusing mode.

Raman Spectroscopy:

Raman spectroscopy is one of the important techniques to study metal oxides and carbon-based materials. The material analysis by this spectroscopy is based on the Raman effect.where in energy shift arises due to inelastic scattering of photon/light by matter and includes energy exchange between sample and incident photon. Two types of inelastic scattering are possible in Raman spectroscopy, such as Stokes and anti-Stokes scattering. The filtration of Stokes and anti-Stokes radiations from the excited sample and analysis gives Raman spectra [9]. In the present thesis, a Horiba Xplora plus V1.2 Multiline confocal Raman spectrometer was employed for all samples with an excitation wavelength of 532 nm.

FT-IR Spectroscopy:

All FT-IR studies were carried out using PerkinElmer Spectrum 1000 FT-IR Spectrometer. The samples for FT-IR were made as pellets by crushing a pinch of samples with high pure KBr (99.9 %) followed by pressing to pellets in hydraulic press.

X-ray photoelectron spectroscopy (XPS):

X-ray photoelectron spectroscopy is a surface-sensitive quantitative spectroscopic technique, which identifies the elements on the sample surface including their chemical nature and oxidation states [10]. X-ray photoelectron spectroscopy data were obtained by Kratos X-ray Photoelectron Spectrometer – Axis Ultra DLD. The powder and film samples have been used for XPS.

Field Emission Scanning Electron Microscopy (FE-SEM) with energy dispersive X-Ray spectroscopy (EDS):

The morphology of all materials within the size range of 200-10 μm was analysed using FESEM (Tescan-Mira 3 LMH). The scanning electron microscopy produces images by the interaction of electron beam with atoms, and once the beam hits the sample material, it generates various kinds of electrons such as Auger, backscattered, secondary, transmitted and diffracted electrons. The analysis of various kinds of secondary electrons from the sample surface gives contrast corresponding to morphology. Energy dispersive X-Ray spectroscopy (EDS) was taken by Quantax 200 using Peltier cooled Silicon drift detector (SDD) system. EDS is based on analyzing unique X-ray emission of elements. The energy of this X-ray is unique to the specific element and transition. The distribution of various elements in the

sample was acquired by the selected area elemental mapping using a specific Xray emission line from the respective elements.

Transmission Electron Microscopy (TEM):

The sample images within the size range 5-100 nm analysis was carried out by TALOS F200S G2 TEM. In this technique, electron beams are transmitted through the sample and then focussed on the imaging device to form images. Selected area electron diffraction (SAED) patterns were taken for the catalyst to confirm the crystal structure in a small area.

Electrochemical characterisation:

Generally, the behaviour of electrocatalysts has been analysed using various electrochemical techniques [11]. All electrochemical studies were carried out using CHI 760 instrument with a three-electrode set-up.

Cyclic voltammetry (CV):

In CV, the potential of the working electrode is ramped from one potential to another in the forward direction, followed by ramping in the opposite direction, with the observation of potential vs current. The observation of a peak with a positive current indicates oxidation, and a negative current peak indicates reduction. CV test of electrocatalysts was carried out to calculate active sites and electrochemical surface area.

Linear sweep voltammetry (LSV):

LSV is half cycle of the cyclic voltammetry. The electrocatalytic activity of irreversible reactions such as oxygen & hydrogen evolution reactions, urea electrochemical oxidation were carried out using LSV study.

Tafel slope:

Tafel slope (b) is useful to understand the kinetics of electrochemical reactions. This slope was obtained by plotting log(current density) vs over potential. A lower value of the Tafel slope represents faster kinetics for electrochemical reactions.

Electrochemical impedance study (EIS):

The electrochemical impedance study is used to measure the impedance of the electrochemical system. This technique implies an application of small AC potential

perturbation in the form of a sinusoidal wave over a range of frequencies. The observable impedance at a particular frequency is related to the process occurring at the particular time scale, which is inverse to that frequency (e.g., frequency of 100 Hz, t = 0.01 s). This technique is widely applicable to understand the number of processes that happen on the electrode-electrolyte interfaces during the reaction. The impedance spectra study was carried out using AC potential perturbation of ± 5 mV for all samples in the frequency range of 10^{-2} to 10^{6} Hz.

Chronoamperometry:

In this technique,the potential of the working electrode is stepped to a particular voltage and measurement of current with the function of time. The catalyst degradation and activity loss can be monitored from the reduction of current at a particular working voltage with the function of time.

Chapter 3: Pd nanoparticles on a coordination polymer-based graphene composites for sustainable electrochemical hydrogen evolution reaction

The organic coordination polymers (CP) have the advantages such as 2D structure with high surface area and effective coordination to metal or its ions for stabilisation [12]. Although CP has many wonderful properties, its catalytic application is limited by a lack of electrical conductivity, so the synthesis of CP with effective conductivity is one of the challenges that has to be addressed. Here, we have studied the electrochemical hydrogen evolution activity of CP compounds based on Pd ions coordinated to benzenetetramine (Pd(BTA) synthesized by C. V. Yelamaggad and co-workers [13]. This was combined with reduced graphene oxide (rGO) to enhance conductivity and further reduced with sodium borohydride to obtain more active species, Pd nanoparticles. HER acitiviy of Pd(BTA), $[Pd(BTA)]_{red}$, Pd(BTA)-rGO and $[Pd(BTA)\text{-}rGO]_{red}$ are shown in Fig. 3 for comparison .

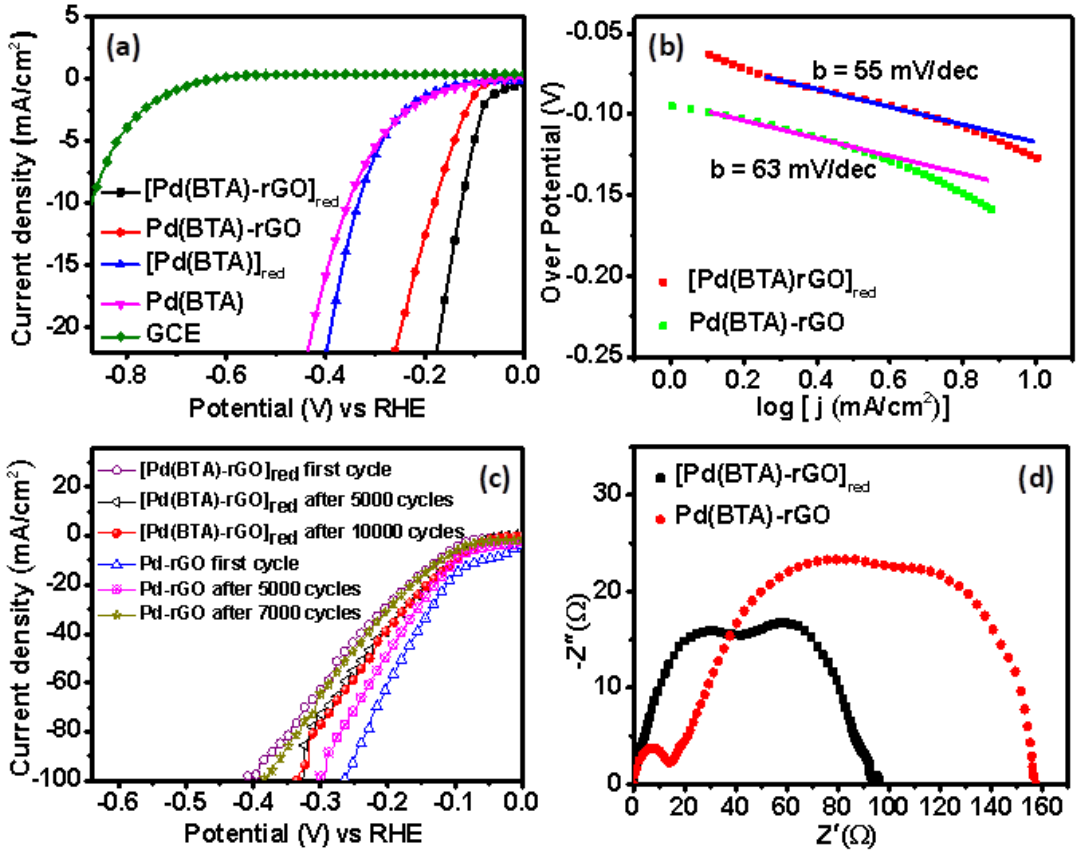

Figure 3: (a) Linear sweep voltammetry of synthesised coordination polymers coated on to glassy carbon electrode (GCE) in 0.5 M H_2SO_4 at a scan rate of 5 mV/s (b) Tafel slope of Pd(BTA)-rGO systems (c) Hydrogen evolution activity comparison of coordination polymer-rGO with Pd-rGO under potential cycling (d) Impedance spectra of Pd(BTA)-rGO systems at −0.12 V vs RHE.

The catalyst ink is prepared by dispersing 1 mg of catalysts in 200 μL of deionised water and 50 μL of isopropyl alcohol followed by sonication for half an hour. The 5 μL of prepared ink was drop cast on glassy carbon electrode for electrochemical studies. The linear sweep voltammetry (LSV) of all Pd based systems were carried out in 0.5 M H_2SO_4 solution. The bare GCE shows negligible current density till an applied potential of -0.7 V vs RHE and hence, has negligible contribution to HER activity. $[Pd(BTA)\text{-}rGO]_{red}$ shows high HER current density at a fixed potential than others (Fig. 3a). Tafel slope (*b*) studies reveal fast HER kinetics of $[Pd(BTA)\text{-}rGO]_{red}$ with a lower *b* value (Fig. 3b). The HER current density of $[Pd(BTA)\text{-}rGO]_{red}$ improves with electrochemical cycling, and it is probably due to the formation of Pd nanoparticles during HER (Fig. 3c). The HER activity comparison of Pd-rGO, obtained by reduction of Pd^{2+} salt in presence of rGO, with $[Pd(BTA)\text{-}rGO]_{red}$ indicates that Pd nanoparticles are stabilised better by Pd(BTA) and rGO sheets than in the case of Pd-

rGO, as observed from the current density reduction of Pd-rGO at a particular potential during electrochemical cycling (Fig. 3c). Impedance study at −0.12 V vs RHE gives lower charge transfer resistance for $[Pd(BTA)\text{-}rGO]_{red}$ than Pd(BTA)-rGO (Fig. 3d).

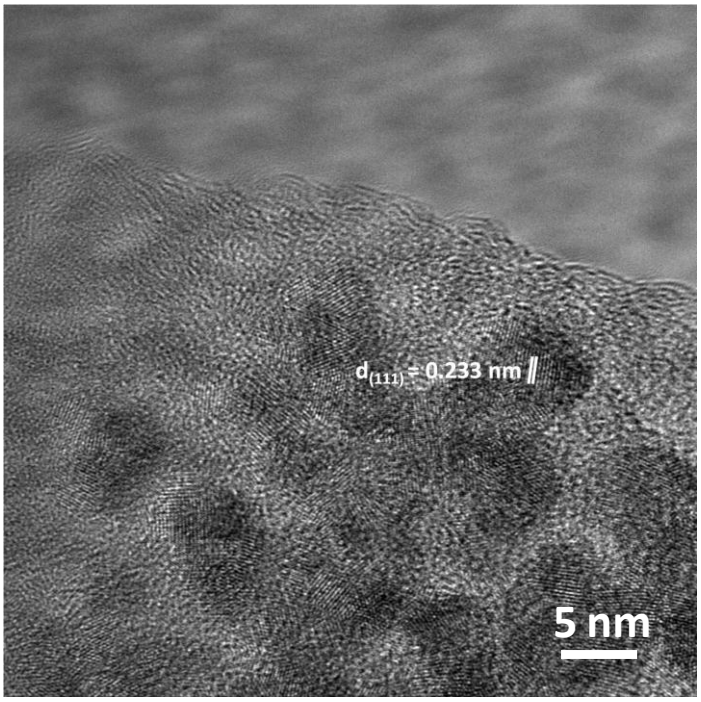

Figure 4: HR-TEM image of $[Pd(BTA)\text{-}rGO]_{red}$.

The HR-TEM image indicates the presence of Pd nanoparticles (size ~3-5 nm) on 2D sheets of Pd(BTA) & rGO after reduction (Fig. 4). The lattice fringes with *d* spacing of 0.233 nm belongs to (111) plane of face centered cubic Pd.

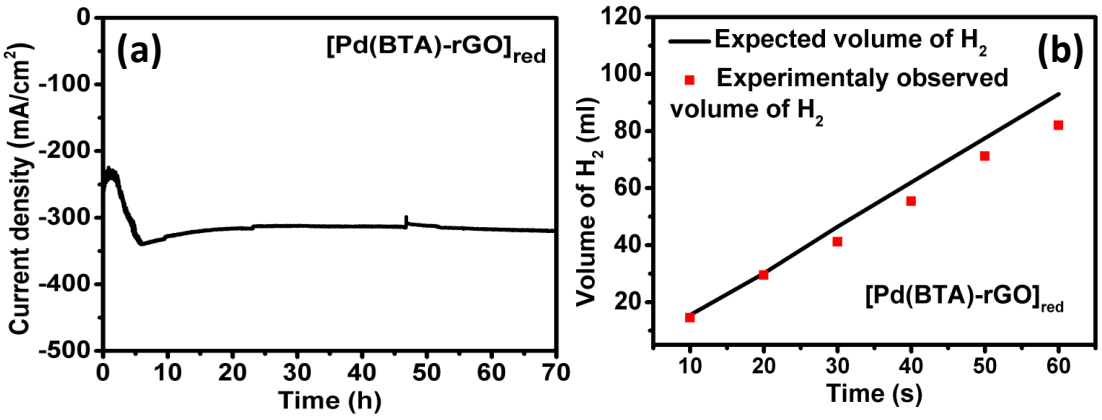

Figure 5: (a) Chronoamperometry study of $[Pd(BTA)\text{-}rGO]_{red}$ at −0.75 V vs RHE, (b) Plot represents the amount of H_2 collection with time during HER for $[Pd(BTA)\text{-}rGO]_{red}$ at −0.78 V vs RHE.

Fig. 5a represents excellent stability of $[Pd(BTA)\text{-}rGO]_{red}$ for 70 h at a current density of ~ −300 mA/cm^2 indicating sustained HER. The Pd nanoparticles of size ~3-5 nm encapsulated within the wide-surface-area of 2D sheets (layers) of coordination polymer and reduced graphene oxide are responsible for the excellent HER activity and stability of the catalyst. The calculated Faradaic efficiency of highly active $[Pd(BTA)\text{-}rGO]_{red}$ is 88.1 % (Fig. 5b).

Chapter 4: The rivalry of oxygen defects and Co^{3+}-reducibility in Co_3O_4 system for oxygen evolution reaction

The Co_3O_4 system is an earth-abundant metal oxide for efficient electrochemical oxygen evolution reaction. . In Co_3O_4 systems, the oxygen vacancy is reported to improve the oxygen evolution reaction activity because of higher Co^{2+}/Co^{3+} surface ratio [14]. Recent in-situ X-ray absorption studies of this material have revealed that in Co-oxide systems readily form 3D cross-linked $Co^{3+/4+}O_x(OH)_y$ species with μ_2-OH bridge during OER and its effective reduction in the sequence, $Co^{4+} \rightarrow Co^{3+} \rightarrow Co^{2+}$ (Co^{3+}-reducibility) mainly decides their activity [15]. In order to resolve these debates on OER active sites, we have synthesised two Co_3O_4 systems by hydrothermal method. Among them, *c*-Co_3O_4, has more oxygen-deficient defects (high Co^{2+}/Co^{3+} ratio) and less Co^{3+}-reducibility while *n*-Co_3O_4 has less oxygen deficient defects (low Co^{2+}/Co^{3+} ratio) and more Co^{3+}-reducibility. Finally, the OER activity of these two systems were studied to understand the real active sites.

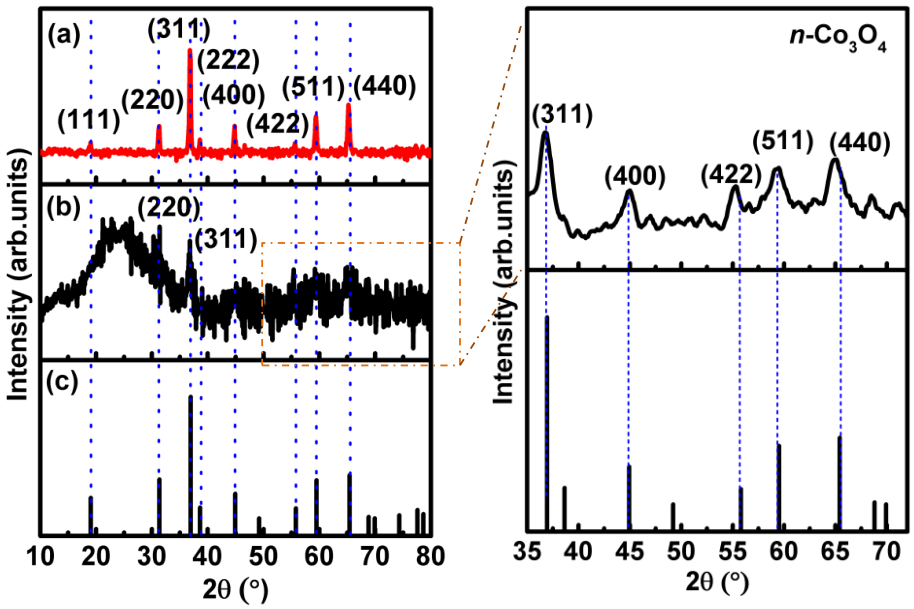

Figure 6: (a) and (b) XRD of *c*-Co_3O_4 and *n*-Co_3O_4 (c) Simulated XRD of Co_3O_4.

The X-ray diffraction of the two cobalt oxide-based systems such as *c*-and *n*-Co_3O_4 show peaks corresponding to spinel Co_3O_4. Intense diffraction peaks that appear at 19.0°, 31.3°, 36.5°, 38.6°, 44.7°, 55.7°, 59.4°, 65.2° correspond to (111), (220), (311), (222), (400), (422), (511), (440), respectively and are in accordance with the standard XRD pattern of Co_3O_4 (Fig. 6a-c). A magnified view and smoothened XRD of the marked region of *n*-Co_3O_4 is shown alongside.

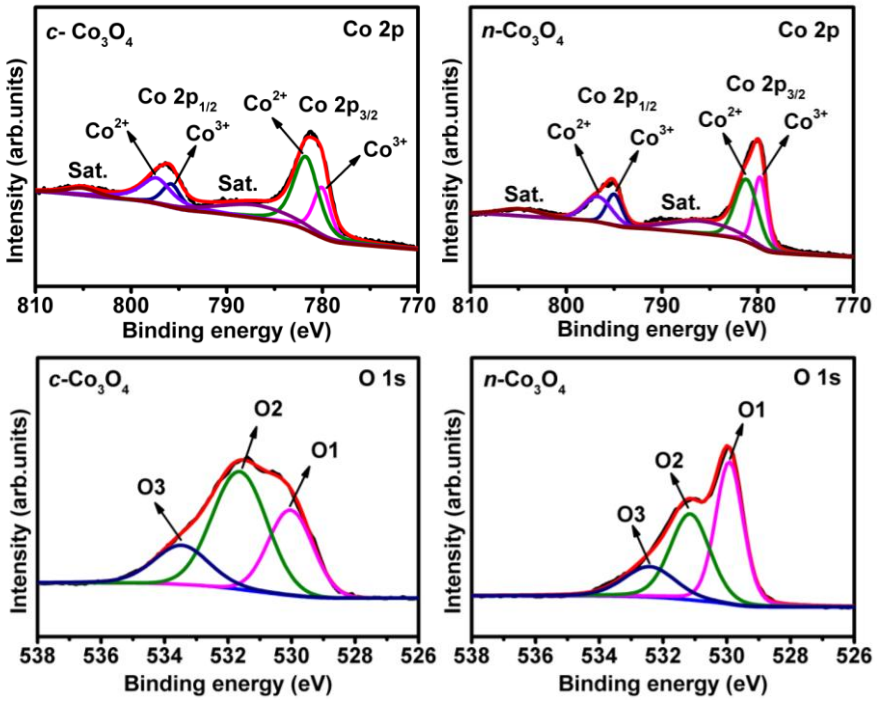

Figure 7: Co 2p and O 1s XPS of *c*- & *n*-Co_3O_4 (O1 – lattice oxygen, O2 -Defective sites oxygen with lower coordination, O3 - Surface adsorbed oxygen species).

The Co 2p spectra of *c*- and *n*-Co_3O_4 systems are fitted with contributions from Co^{2+} and Co^{3+} ions and the *c*-Co_3O_4 gives Co^{2+}/Co^{3+} peak intensiy ratio of 1.93 wherein *n*-Co_3O_4, it is 1.46 (Fig. 7). The higher amount of oxygen deficient defects in *c*-Co_3O_4 are further supported by the enhancement of O2 peak in *c*-Co_3O_4 (Fig. 7) [14].

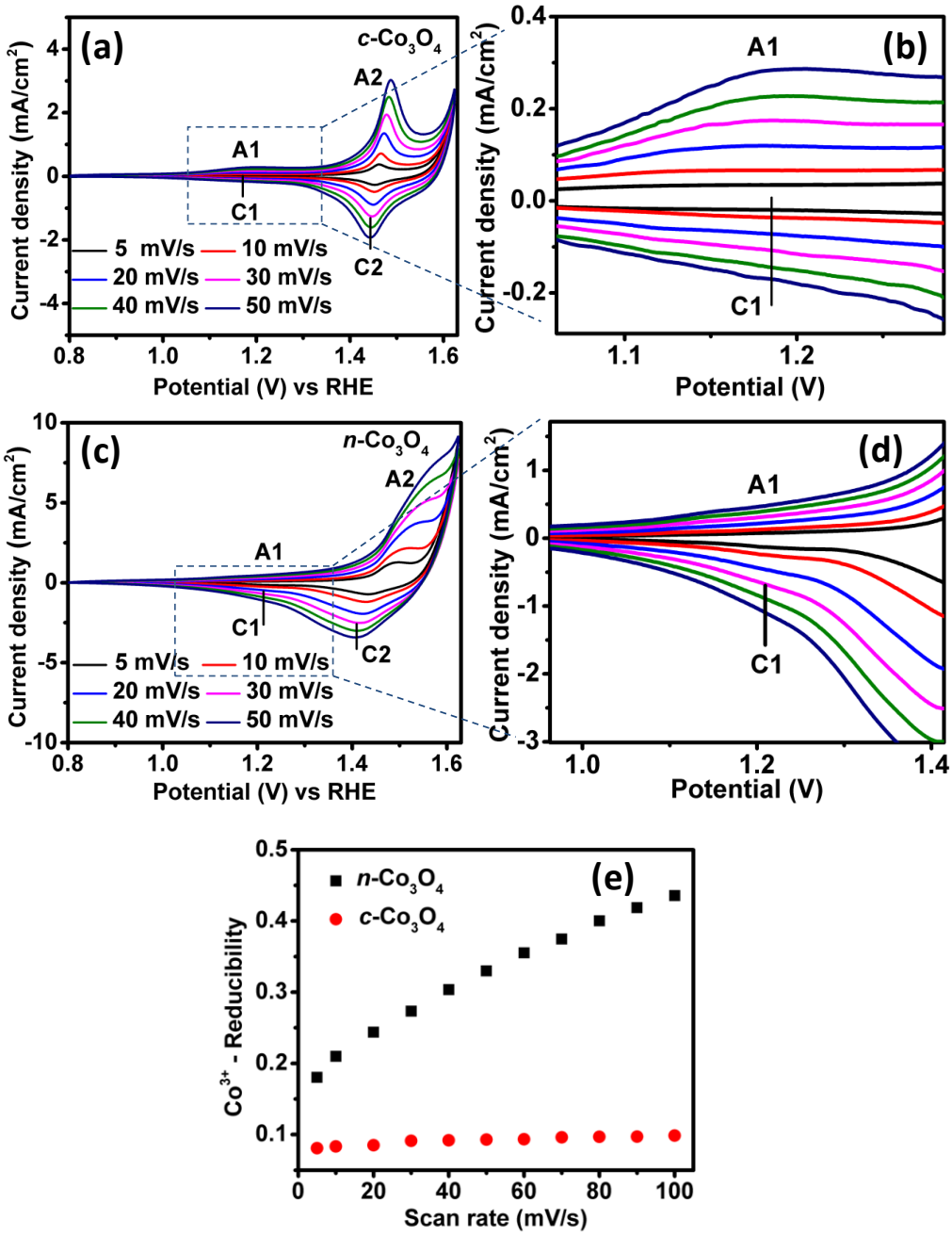

Figure 8: (a) & (c) Cyclic voltammetry of *c*- and *n*-Co_3O_4 at various scan rates in 1 M KOH solution. (b) & (d) magnified view of the marked regions in figure (a) & (c). (e) Co^{3+}-reducibility comparison of *c*- & *n*-Co_3O_4 (A1 is $Co^{2+} \rightarrow Co^{3+}$ oxidation, A2 is $Co^{3+} \rightarrow Co^{4+}$oxidation, C2 is $Co^{4+} \rightarrow Co^{3+}$ reduction, C1 is $Co^{3+} \rightarrow Co^{2+}$ reduction).

The cyclic voltammetry of compounds *c*- & *n*-Co_3O_4 at different scan rates were carried out in 1 M KOH solution, followed by calculation of Co^{3+}-reducibility using the formula, Co^{3+} -reducibility = double-layer corrected (C1/C2) current ratio as shown in the Fig. 8(a-e) [15]. The compound *n*-Co_3O_4 shows more Co^{3+} reducibility than c-Co_3O_4 at different scan rates

(Fig. 8e). Hence, it is shown here that *c*-Co_3O_4, has more Co^{2+}/Co^{3+} ratio and less Co^{3+} reducibility and *n*-Co_3O_4, has less Co^{2+}/Co^{3+} ratio and more Co^{3+}-reducibility.

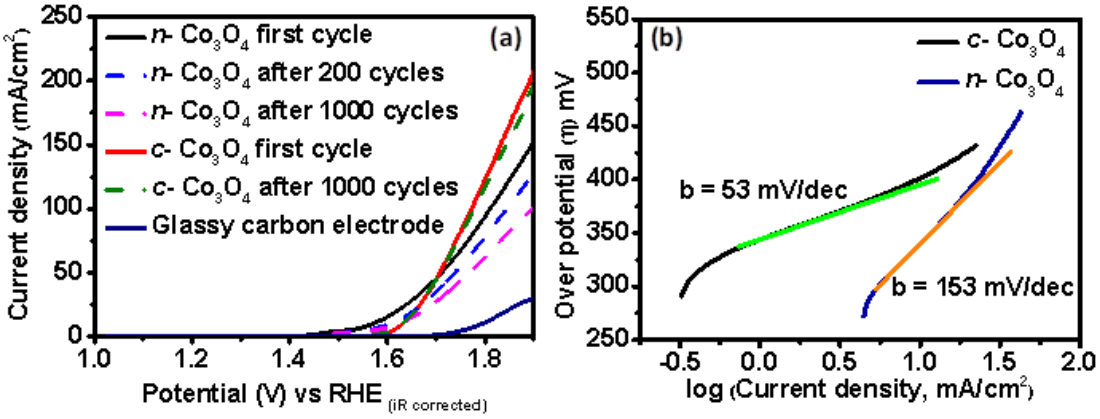

Figure 9: (a) iR corrected linear sweep voltammetry of *c*- & *n*-Co_3O_4 in 1 M KOH solution at a scan rate of 5 mV/s. (b) Tafel slope of *c*- & *n*-Co_3O_4.

The linear sweep voltammetry (LSV) study shows compound with higher Co^{3+}-reducibility (*n*-Co_3O_4) exhibits OER current at a lower potential than a compound that has more oxygen-deficient defects (*c*-Co_3O_4) (Fig. 9a). It can be noticed that bare GCE has little contribution to OER activity at applied potentials less than 1.8 V. Tafel slope (*b*) reveals *n*-Co_3O_4 follows slow kinetics than *c*-Co_3O_4 (Fig. 9b). The higher Tafel slope of *n*-Co_3O_4 is attributed to the reduction in kinetics due to considerable adsorption capacitance associated with surface irregularity, pores and Co^{3+}-Oh site. The higher surface defects, and fine morphology are responsible for faster kinetics and lesser Tafel slope for OER in *c*-Co_3O_4. Both the systems follow different kinetics for OER and *n*-Co_3O_4 showing higher current at the lower potential is a good catalyst at lower OER region while crystalline Co_3O_4 is a good catalyst for higher OER region with maximum current density 220 mA/cm^2 at 1.92 V. The study presents possible future directions to tailor-made Co_3O_4 based catalyst with Co^{3+}-Oh sites having higher reducible nature prone to less adsorption capacitance.

Chapter 5: Role of metal ion sites in bivalent cobalt phosphorus oxygen systems towards efficient oxygen evolution reaction

In the recent studies on various cobalt phosphates as oxygen evolution reaction (OER) catalysts, the influence of ligands for efficient proton abstraction has been highlighted to account for the observed higher activity [16]. The role of CoO(OH) active sites has not been given sufficient importance to compare the activity in these systems. In order to explain the OER activity in relation to metal ion sites, we have synthesised three different cobalt phosphorous oxyanion systems such as $NaCoPO_4$ (CP-1), $Co_{11}(HPO_3)_8(OH)_6$ (CP-2), and $Co_3(OH)_2(HPO_4)_2$ (CP-3) by changing the molar ratio of $Na_4P_2O_7$ and $CoCl_2.6H_2O$ employing the hydrothermal method. We have shown that the OER activity of these compounds can be correlated with the average number of $CoO_x(OH)_y$ reduction sites in the $Co^{4+} \leftrightarrow Co^{3+} \leftrightarrow Co^{2+}$ sequence.

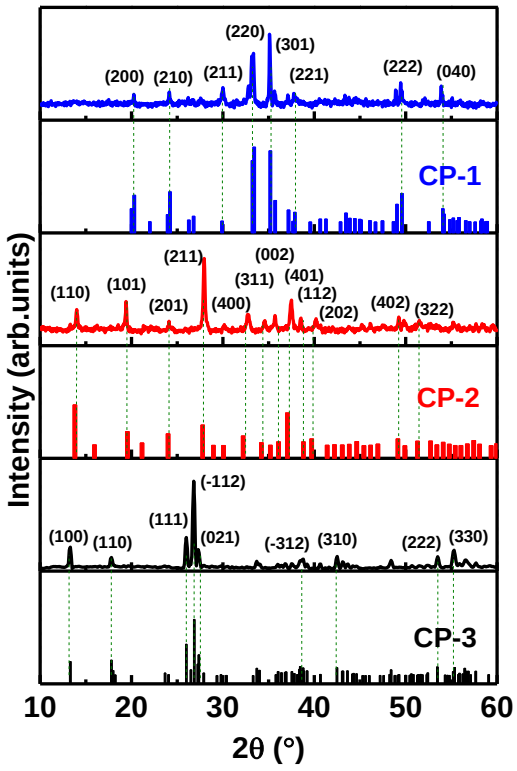

Figure 10: XRD of three different cobalt phosphorous oxygen systems obtained by hydrothermal reaction along with the respective simulated patterns.

The X-ray diffraction patterns of the three cobalt phosphates such as $NaCoPO_4$, $Co_{11}(HPO_3)_8(OH)_6$ and $Co_3(HPO_4)_2(OH)_2$ can be compared with simulated patterns and confirm the formation of the above phosphates (Fig. 10). The crystal structure of CP-1 (α-$NaCoPO_4$) contains the edge-sharing chain of CoO_6 octahedra cross-connected by PO_4 tetrahedra. This arrangement forms ten coordinate cavities in which Na^+ ions are located. The compound CP-2 ($Co_{11}(HPO_3)_8(OH)_6$) has infinite $(Co_4O_{12})_n$ double chains built up by dimeric Co_2O_9 entities consisting of face-sharing of two CoO_6 octahedra and linked through two common edges. The final three-dimensional arrangements of octahedra are formed by corner-sharing of each Co_4O_{12} to other four equivalent ones. In the resulting hexagonal structure, two kinds of channels are available, smaller triangular one occupied by the 2/8 pseudo tetrahedral HPO_3^{2-} groupand a larger hexagonal channel occupied by the 6/8 HPO_3^{2-} group. In the CP-3 ($Co_3(OH)_2(HPO_4)_2$) structure, the CoO_6 (1) octahedron sharing its opposite face with CoO_6 (2) octahedron forms the Co_3O_{12} group and is linked to HPO_4^{2-} tetrahedron, resulting in the formation of corrugated layers.

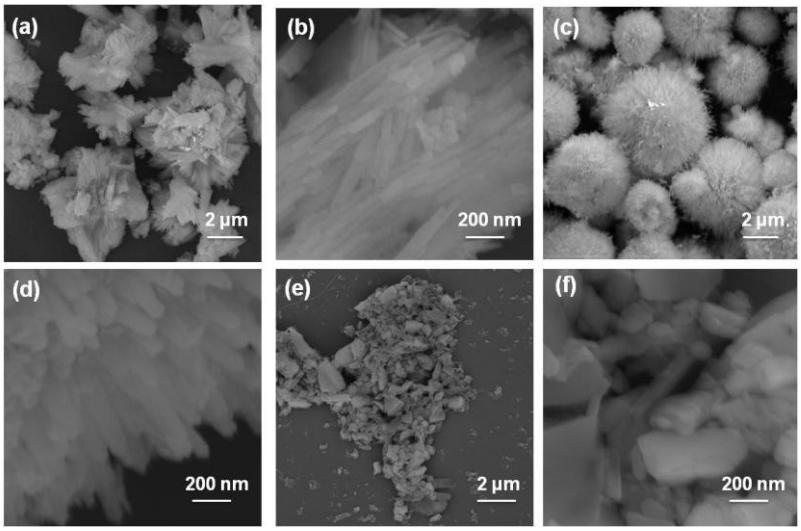

Figure 11: FESEM images of the as-synthesized Co phosphorous oxy anion compounds (a,b) CP-1, (c,d) CP-2, and (e,f) CP-3.

The morphological analysis of CP-1 shows bundled nanobelt-like structures (Fig. 11a,b) while CP-2 shows three-dimensional structures with flower-like morphology consisting of nanorod bunches (Fig. 11c,d). CP-3 consists of aggregated flakes or platelets (Fig. 11e,f).

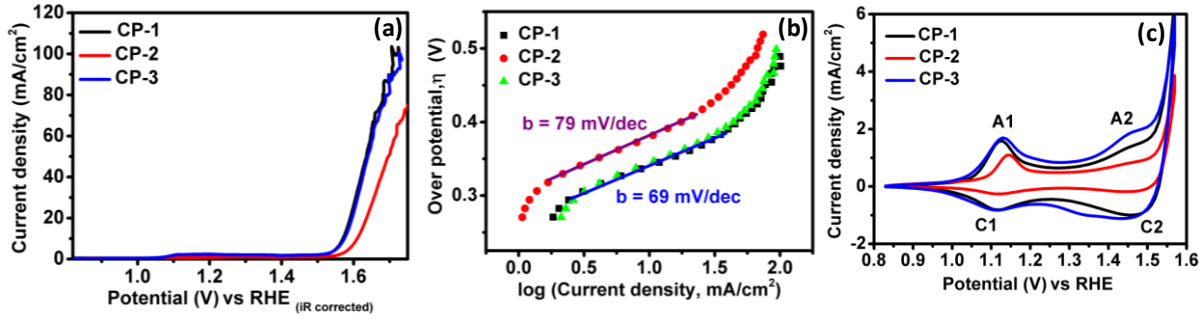

Figure 12: (a) & (b) LSV and Tafel slope of three different cobalt phosphorous oxygen systems in 1 M KOH solution at a scan rate of 5 mV/s, (c) Cyclic voltammetry (CV) of cobalt phosphorous oxygen systems at a scan rate of 10 mV/s (A1 is $Co^{2+} \rightarrow Co^{3+}$ oxidation, A2 is $Co^{3+} \rightarrow Co^{4+}$oxidation, C2 is $Co^{4+} \rightarrow Co^{3+}$ reduction, C1 is $Co^{3+} \rightarrow Co^{2+}$ reduction).

The linear sweep voltammetry and Tafel slope analysis of the cobalt phosphorous oxygen systems indicate that the the OER activity of the systems follows as CP-1 ~ CP-3 > CP-2 (Fig. 12a & b). The CV of the compounds (Fig. 12c) gives two oxidation (A1 & A2) and two reduction peaks (C1 & C2) of Co^{2+} ions in the redox sequence $Co^{2+} \leftrightarrow Co^{3+} \leftrightarrow Co^{4+}$ [15]. Estimation of the average number of Co^{3+} and Co^{2+} ions from C2 and C1 peaks by integration gives the same values for CP-1 & CP-3 ~ 5.1 nanomoles, whereas CP-2 gives the lower value of 1.53 nanomoles. The OER activity trend is in agreement with the effective no. of Co^{3+} and Co^{2+} ions (formed during OER) of the cobalt phosphorous oxygen systems. The study reveals that in cobalt phosphorous oxyanion systems, though the proton abstracting -PO_x ligands can promote OER kinetics via proton coupled electron transfer step (PCET), metal or active sites decide their overall activity rather than the coordinating ligands. This is demonstrated by comparing OER activity of $NaCoPO_4$ (CP-1), $Co_{11}(HPO_3)_8(OH)_6$ (CP-2), and $Co_3(OH)_2(HPO_4)_2$ (CP-3) and analyzing the electrochemical data in detail. The observed OER current density and Tafel slope-based activity of the bivalent cobalt phosphorous oxy anion systems under study can be explained in terms of the number of effective sites involved in the $Co^{2+} \leftrightarrow Co^{3+} \leftrightarrow Co^{4+}$ redox sequence as the OER descriptor following the activity trend, CP-1 ~ CP-3 > CP-2. The other OER activity parameters, such as lower charge transfer resistance (102 Ω) and high turn over frequency (0.038266 s^{-1}), are observed for the CP-1 system with almost the same overpotential (340 mV) and Tafel slope (69 mV/ dec) values as CP-3. The above mentioned evaluation underlines the importance of choosing suitable cobalt-based phosphorous oxyanion systems with more number of effective active sites.

Chapter 6: Introduction of surface defects in NiO and effective removal of adsorbed catalyst poisons for improved electrochemical urea oxidation reaction

The electrochemical urea oxidation reaction (UOR) is a promising low-cost method to replace water oxidation reaction for low energy electrochemical hydrogen production [17]. The important factors to be considered in order to attain better UOR efficiency are electrocatalyst design by tuning defects, surface area and effective removal of CO_2 poisoning on the catalyst surface [18]. In this study, we have prepared surface oxidised NiO (e-NiO) with surface defects by electron beam bombardment. The enhancement of NiO(OH) active species and the effect of surface defects on UOR have been analysed.

The NiO was synthesised by annealing of $Ni(OH)_2$ at 650 °C for 3 h in air. The formed NiO is pelletized, fused at high temperature (1000 °C) and subjected to electron beam treatment for introducing defects.

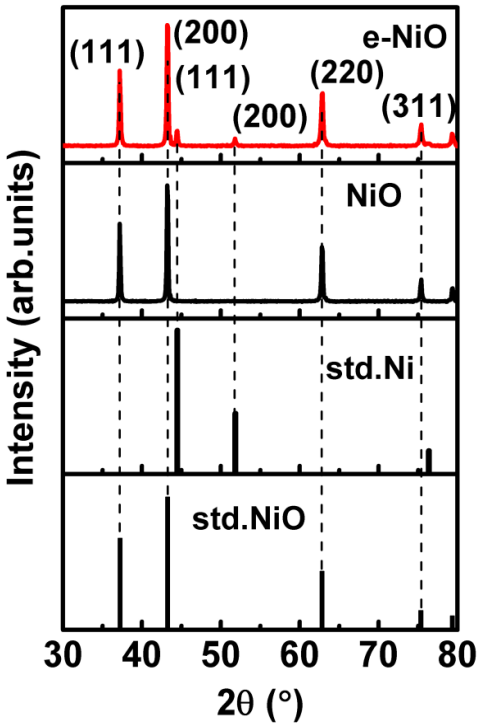

Figure 13: XRD patterns of pristine NiO and electron bombarded NiO (e-NiO) with simulated standard XRD patterns of NiO and Ni.

XRD pattern of pristine NiO sample show peaks corresponding to the planes of fcc structure of NiO. After electron beam bombardment of NiO, e-NiO shows additional low intense peaks corresponding to fcc Ni along with that due to NiO (Fig. 13). The calculated average crystalline size of pristine NiO is 45.42 nm, which reduces to 36.81 nm after electron bombardment. These are calculated from XRD using Scherrer equation $D = k.\lambda/(\beta.\text{Cos}\theta)$, λ – X ray wavelength, D – grain size in nm, k-Scherrer constant 0.9, β – full wave half maximum, θ – peak position in radians.

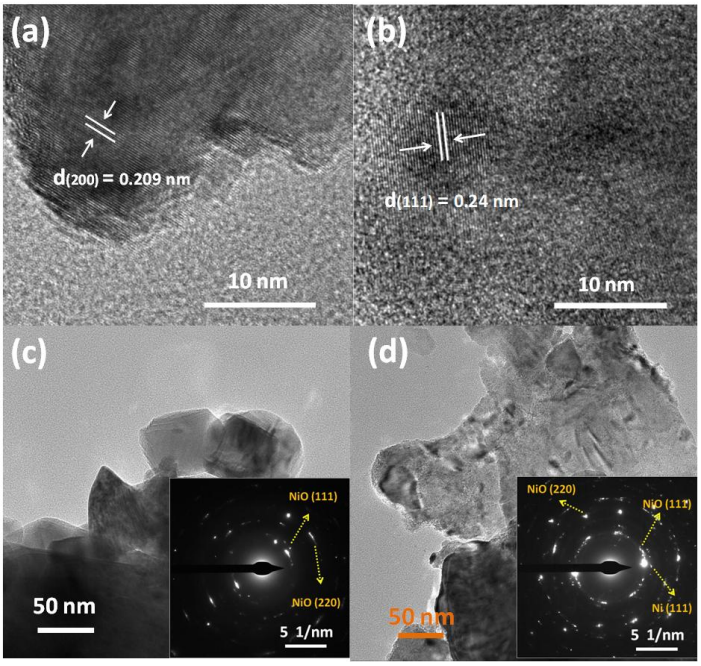

Figure 14: High resolution TEM images (a,c) pristine NiO and (b,d) e-NiO. Insets in (c) and (d) give SAED pattern from the respective samples.

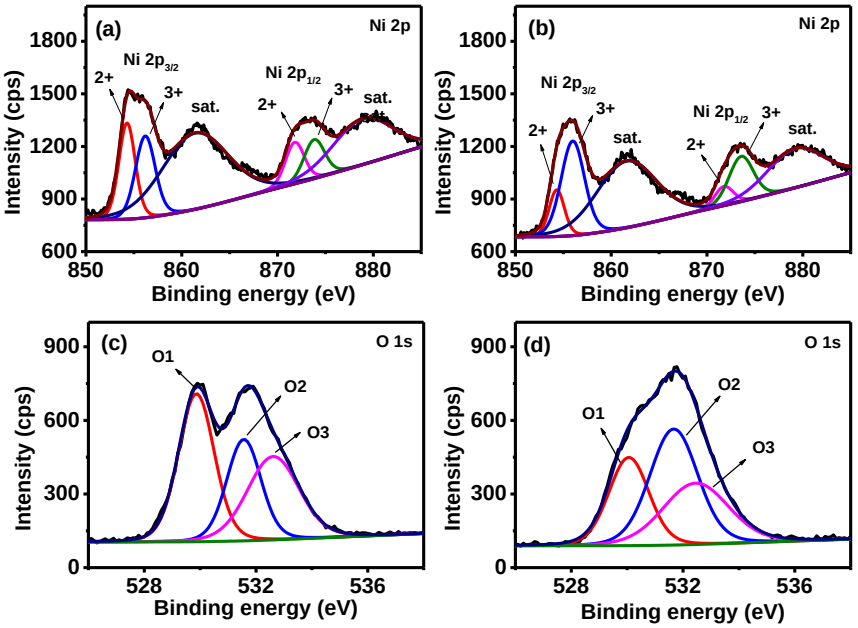

Figure 15: XPS spectra of pristine NiO and e-NiO (a) Ni 2p spectra and (c) O1s spectra of pristine NiO. (b) Ni 2p and (d) O1s spectra of e-NiO (O1 - lattice oxygen, O2 - Defective sites oxygen with lower coordination, O3 - Surface adsorbed oxygen Species).

TEM images show aggregated crystallites of NiO in both samples (Fig. 14) and might be due to the high-temperature sintering of samples. The lattice spacing of 0.209 nm and 0.24 nm is observed for NiO and e-NiO samples, which belong to (200) and (111) planes of fcc NiO (Fig. 14a & b). The selected area electron diffraction (SAED) shows diffraction spots belonging to (111), (220) planes of NiO (Fig. 14c inset) and additional diffraction due to of Ni (111) in e-NiO sample (Fig. 14d inset).

The XPS Ni 2p spectra of NiO and e-NiO can be fitted with contributions from Ni^{2+} and Ni^{3+} ions [19] and the ratio of Ni^{3+}/Ni^{2+} peak intensity is 3.1 for NiO, which is almost 3 times of that observed for the pristine case (1.03) (Figure 15). This reveals that electron beam bombardment introduces a significant number of Ni^{3+} sites on NiO surface. The enhancement of O2 peak in e-NiO than NiO further confirms surface defects.

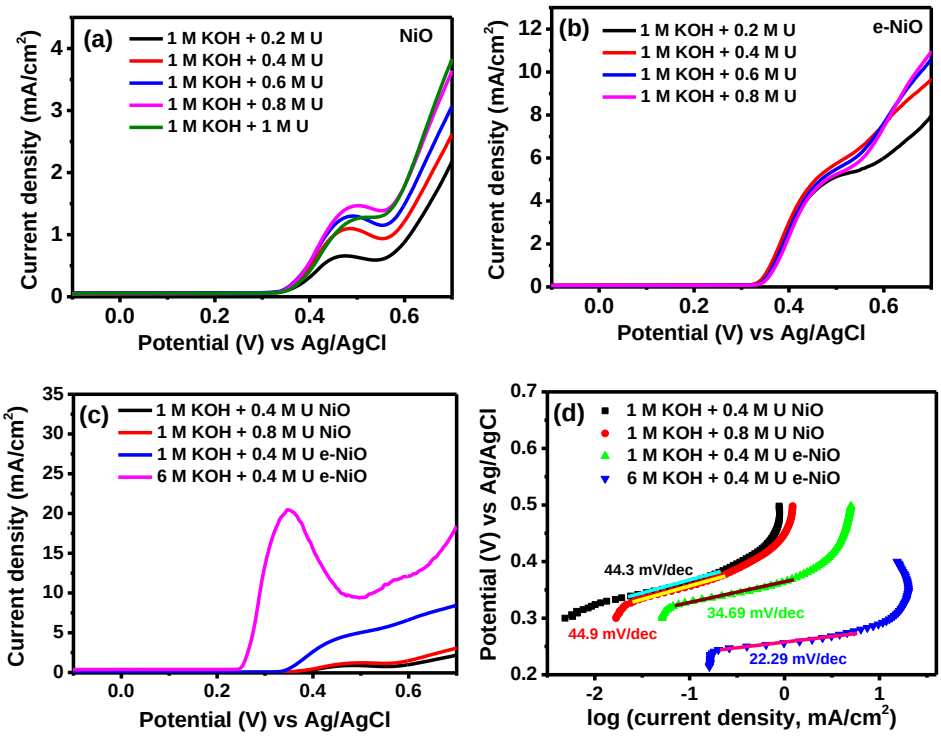
(a)
NiO
1 M KOH + 0.2 M U
1 M KOH + 0.4 M U
1 M KOH + 0.6 M U
1 M KOH + 0.8 M U
1 M KOH + 1 M U
Current density (mA/cm²)
Potential (V) vs Ag/AgCl
(b)
e-NiO
1 M KOH + 0.2 M U
1 M KOH + 0.4 M U
1 M KOH + 0.6 M U
1 M KOH + 0.8 M U
Current density (mA/cm²)
Potential (V) vs Ag/AgCl
(c)
1 M KOH + 0.4 M U NiO
1 M KOH + 0.8 M U NiO
1 M KOH + 0.4 M U e-NiO
6 M KOH + 0.4 M U e-NiO
Current density (mA/cm²)
Potential (V) vs Ag/AgCl
(d)
1 M KOH + 0.4 M U NiO
1 M KOH + 0.8 M U NiO
1 M KOH + 0.4 M U e-NiO
6 M KOH + 0.4 M U e-NiO
44.3 mV/dec
44.9 mV/dec
34.69 mV/dec
22.29 mV/dec
Potential (V) vs Ag/AgCl
log (current density, mA/cm²)

Figure 16: Linear sweep voltammograms of (a) Pristine NiO and (b) e-NiO modified glassy carbon electrode (GCE) acquired at a scan rate of 10 mV/s in various urea (U) concentration and 1 M KOH (c) Comparative LSVs of pristine NiO and e-NiO at a scan rate of 5 mV/s in urea-KOH solutions in which they have exhibited high activity (d) Tafel slope of pristine NiO and e-NiO corresponding to LSVs in (c).

The UOR activity of samples, NiO and e-NiO are studied by increasing urea (U) concentration gradually at constant KOH (1 M) (Fig. 16a & b). NiO exhibits current density improvement till 0.8 M U, where as in e-NiO initially, a slight UOR current improvement is observed from 0.2 to 0.4 M U and thereafter the current density is constant with increase in urea concentration (Fig. 16b). The UOR activity of e-NiO further improved by using 0.4 M U and 6 M KOH electrolyte (Fig. 16c). The UOR current comparison of both NiO and e-NiO with its Tafel slope values are given in Fig. 16d. e-NiO shows maximum current density and lower Tafel slope than NiO (Fig. 16) and indicates its better catalytic activity.

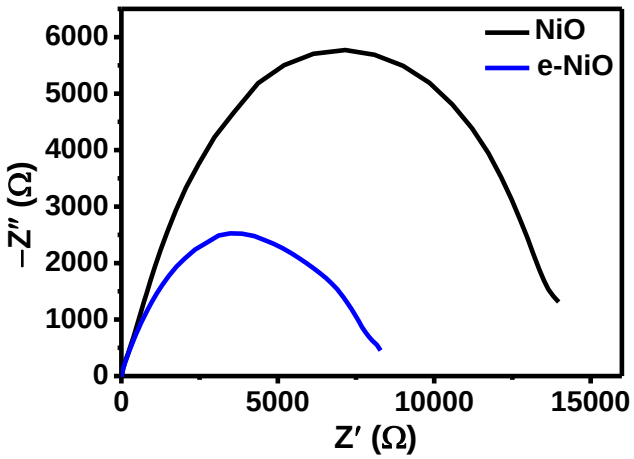

Figure 17: Impedance spectra of NiO and e-NiO at 0.36 V in 0.4 M U + 1 M KOH solution.

The impedance spectra of NiO and e-NiO at 0.4 M U + 1 M KOH solution, represents higher charge transfer resistance for NiO than e-NiO (Fig. 17). The lower charge transfer resistance is an indication of faster kinetics, supported by lower tafel slope value of e-NiO (Fig. 16d).

We show that electron beam bombardment on NiO (e-NiO) generate surface defects in the catalyst with improvement of surface Ni^{3+}/Ni^{2+} ratio beneficial for NiO(OH) active species generation and urea surface adsorption resulting in enhanced urea oxidation reaction (UOR). This is corroborated by high UOR current density and lower Tafel slope in 0.4 M urea containing 1 M KOH electrolyte solution obtained for e-NiO compared to pristine NiO. Higher number of surface active species and efficient urea adsorption cause enhanced release of CO_2 resulting in dominant surface poisoning, a main hindrance to UOR kinetics. The improvement of UOR current (20.74 mA/cm^2) and lower Tafel slope from 34 to 22 mV/dec in 6 M KOH with 0.4 M urea solution indicates removal of CO_2 poision and high activity. This study projects the significance of effective removal of CO_2 surface poison for improving

UOR while promoting surface active sites employing appropriate KOH and urea concentrations.

Chapter 7: Conclusions & future scope

In conclusion, in this thesis work we have addressed catalyst activity descriptor, stability, active site enhancement factors and ways of tuning the materials for fruitful applications by synthesizing specific catalyst systems and studying their electrochemical performance in detail. In the case of Pd based electrocatalyst stability, it is rectified by encapsulating Pd nanoparticles through Pd(BTA) on reduced graphene oxide. In Co_3O_4 system the descriptor for OER activity is proved as Co^{3+}-reducibility. The number of Co^{4+}/Co^{3+} & Co^{3+}/Co^{2+} reduction sites in active species $CoO_x(OH)_y$ explains the better OER activity in bivalent cobalt phosphorous oxyanions systems than ligand effect and Co^{3+} reducibility. e-NiO improves NiO(OH) species with strong adsorption of urea, which leads to CO_x poisoning. The CO_x poisons can be removed by adjusting the molar ratio of urea and KOH.

The organic encapsulation for sustainable electrocatalysis may be applied to other metal based systems to produce highly stable low cost electrocatalyst. In-situ spectroscopic and isotopic studies can be carried out to identify the involvement of HPO_x/PO_x ligands for proton abstraction and lattice oxygen involvement from HPO_x/PO_x during OER. This study can provide the significant insight about the P-O linkage effect on OER activity. The operando spectroscopic studies of e-NiO surface is needed to observe the behaviour of catalyst surface at various urea and KOH concentration in terms of removing the CO_x poisons and supporting the direct UOR mechanism.

List of publications

Following are the publications resulting from the thesis work carried out by the candidate.

1. Role of Metal Ion Sites in Bivalent Cobalt Phosphorus Oxygen Systems toward Efficient Oxygen Evolution Reaction, **C. Alex**, C . Sathiskumar, Neena S. John, *J. Phys. Chem. C*, 2021, 125, 24777–24786.

2. Introduction of surface defects in NiO with effective removal of adsorbed catalyst poisons for improved electrochemical urea oxidation. **C. Alex**, G. Shukla, and Neena S. John, *Electrochim. Acta*, 2021 , 385,138425.

3. Competing effect of Co^{3+} reducibility and oxygen-deficient defects toward high oxygen evolution activity in Co_3O_4 systems in alkaline medium. **C. Alex**, Saurav .Ch., Sarma, Sebastian.C. Peter, and Neena S. John, *ACS Appl. Energy Mater.,* 2020, 3, 5439-5447.

4. Highly efficient and sustained electrochemical hydrogen evolution by embedded Pd-nanoparticles on a coordination polymer—reduced graphene oxide composite. **C. Alex,** Sachin A. Bhat, Neena S. John, and C. V. Yelamaggad. *ACS Appl.Energy Mater.,* 2019,2, 8098-8106.

Other Publications

5. A general route to free-standing films of nanocrystalline molybdenum chalcogenides at a liquid/liquid interface under hydrothermal conditions. Ramya B. Prabhu, Kaushalendra K. Singh, **C. Alex**, and Neena S. John. *Appl. Surf. Sci.* 2020, 511, 145579.

6. Nickel cobalt phosphite nanorods decorated with carbon nanotubes as bifunctional electrocatalysts in alkaline medium with a high yield of hydrogen peroxide. C. Sathiskumar, **C. Alex**, and Neena S. John. *ChemElectroChem,* 2020, 7, 1935-1942.

7. Hybrid films of $Ni(OH)_2$ nanowall networks on reduced graphene oxide prepared at a liquid/liquid interface for oxygen evolution and supercapacitor applications. K. Bramhaiah, **C. Alex,** Vidya N. Singh, and Neena S. John, *ChemistrySelect* 2019, 4, 2519-2528.

8. Designing metallic MoO_2 nanostructures on rigid substrates for electrochemical water activation. R. Vivek, **C. Alex,** Aruna N. Nair, and Neena S. John. *Chemi. Eur. J.,* 2018, 24, 18003-18011.

Bibilography:

1. Sarkar, S. and Peter, S.C., An overview on Pd-based electrocatalysts for the hydrogen evolution reaction. *Inorg. Chem. Front.*, 2018, *5*, pp.2060-2080.
2. Jin, H., Liu, X., Chen, S., Vasileff, A., Li, L., Jiao, Y., and Qiao, S. Z. Heteroatom-doped transition metal electrocatalysts for hydrogen evolution reaction. *ACS Energy Lett.*, 2019, *4*, 805-810.
3. Song, F., Bai, L., Moysiadou, A., Lee, S., Hu, C., Liardet, L., and Hu, X. Transition metal oxides as electrocatalysts for the oxygen evolution reaction in alkaline solutions: an application-inspired renaissance. *J. Am. Chem. Soc.*, 2018, *140*, 7748-7759.

4. Lu, X. F., Zhang, S. L., Sim, W. L., Gao, S., and Lou, X. W. Phosphorized $CoNi_2S_4$ Yolk-Shell Spheres for Highly Efficient Hydrogen Production via Water and Urea Electrolysis. *Angew. Chem. Int. Ed.*, 2021, *60*, 22885-22891.
5. Anantharaj, S., Ede, S. R., Sakthikumar, K., Karthick, K., Mishra, S., and Kundu, S. Recent trends and perspectives in electrochemical water splitting with an emphasis on sulfide, selenide, and phosphide catalysts of Fe, Co, and Ni: a review. *ACS Catal.*, 2016, *6*, 8069-8097.
6. Gottesfeld, S., and Srinivasan, S.Electrochemical and optical studies of thick oxide layers on iridium and their electrocatalytic activities for the oxygen evolution reaction. *J. Electroanal. Chem. Interf. Electrochem.*, 1978, *86*, 89-104.
7. Paul, S.C., Dey, S. C., Molla, M. A., Islam, M. S., Debnath, S., Miah, M. Y., Ashaduzzaman, M., and Sarker, M.,Nanomaterials as electrocatalyst for hydrogen and oxygen evolution reaction: Exploitation of challenges and current progressions. *Polyhedron* 2021, *193*, 114871.
8. Harrington, G. F., and Santiso, J. Back-to-Basics tutorial: X-ray diffraction of thin films.*J. Electroceramics* 2021, 1-23.
9. Graves, P. R. G. D. J., and Gardiner, D. Practical raman spectroscopy. *Springer*. 1989.
10. Hollander, J. M., and Jolly, W. L. X-ray photoelectron spectroscopy. *Acc. Chem. Res.*, 1970, *3*, 193-200.
11. Gouws, S. Voltammetric characterisation methods for the PEM evaluation of catalysts. *Electrolysis*, 2012, 87.
12. Chen, J., Xia, G., Jiang, P., Yang, Y., Li, R., Shi, R., Su, J. and Chen, Q., Active and durable hydrogen evolution reaction catalyst derived from Pd-doped metal–organic frameworks. *ACS Appl. Mater. interfaces*, 2016, *8*, 13378-13383.
13. Bhat, S. A., Palakurthy, N. B., Kambhala, N., Subramanian, A., Shankar Rao, D. S., Krishna Prasad, S., and Yelamaggad, C. V. Gram-Scale Synthesis and Multifunctional Properties of a Two-Dimensional Layered Copper (II) Coordination Polymer. *ACS Appl. Polym. Mater.*, 2020, *2*, 1543-1552.
14. Zhang, G., Yang, J., Wang, H., Chen, H., Yang, J., and Pan, F. $Co_3O_{4-\delta}$ Quantum dots as a highly efficient oxygen evolution reaction catalyst for water splitting. *ACS Appl. Mater. Interfaces* 2017, 9, 16159– 16167.
15. Bergmann, A., Jones, T. E., Martinez Moreno, E., Teschner, D., Chernev, P., Gliech, M., Reier, T., Dau, H., and Strasser, P. Unified structural motifs of the catalytically

active state of Co(oxyhydr)oxides during the electrochemical oxygen evolution reaction. *Nat. Catal.*, 2018, 1, 711.

16. Kim, H., Park, J., Park, I., Jin, K., Jerng, S. E., Kim, S. H., Nam, K. T., and Kang, K. Coordination tuning of cobalt phosphates towards efficient water oxidation catalyst. *Nat. Commun.*, 2015, *6*, 1– 11,
17. Guo, F., Ye, K., Du, M., Huang, X., Cheng, K., Wang, G., and Cao, D. Electrochemical impedance analysis of urea electro-oxidation mechanism on nickel catalyst in alkaline medium. *Electrochim. Acta*, 2016, *210*, 474-482.
18. Hu, X., Zhu, J., Li, J., and Wu, Q. Urea Electrooxidation: Current Development and Understanding of Ni-Based Catalysts. *ChemElectroChem*, 2020, *7*, 3211-3228.
19. Carley, A. F., Jackson, S. D., O'shea, J. N., and Roberts, M. W. The formation and characterisation of Ni^{3+}—an X-ray photoelectron spectroscopic investigation of potassium-doped Ni(110)–O. *Surf. Sci.*,1999, *440*, 868-874.

Signature of Ph.D. Student

Signature of Research supervisor

Forwarded by Head of the Institution